

Neural-network quantum state tomography for many-body systems

Giacomo Torlai,^{1,2,3} Guglielmo Mazzola,³ Juan Carrasquilla,⁴
Matthias Troyer,^{3,5} Roger Melko,^{1,2} and Giuseppe Carleo³

¹*Department of Physics and Astronomy, University of Waterloo, Ontario N2L 3G1, Canada*

²*Perimeter Institute of Theoretical Physics, Waterloo, Ontario N2L 2Y5, Canada*

³*Theoretische Physik, ETH Zurich, 8093 Zurich, Switzerland*

⁴*D-Wave Systems Inc., 3033 Beta Avenue, Burnaby BC V5G 4M9, Canada*

⁵*Quantum Architectures and Computation Group,
Station Q, Microsoft Research, Redmond, WA 98052, USA*

The experimental realization of increasingly complex synthetic quantum systems calls for the development of general theoretical methods, to validate and fully exploit quantum resources. Quantum-state tomography (QST) aims at reconstructing the full quantum state from simple measurements, and therefore provides a key tool to obtain reliable analytics. Brute-force approaches to QST, however, demand resources growing exponentially with the number of constituents, making it unfeasible except for small systems. Here we show that machine learning techniques can be efficiently used for QST of highly-entangled states, in both one and two dimensions. Remarkably, the resulting approach allows one to reconstruct traditionally challenging many-body quantities – such as the entanglement entropy – from simple, experimentally accessible measurements. This approach can benefit existing and future generations of devices ranging from quantum computers to ultra-cold atom quantum simulators.

Machine-learning (ML) methods have been demonstrated to be particularly powerful at compressing high-dimensional data into low-dimensional representations.^{1,2} Thanks to its intrinsic flexibility, ML is being applied to unravel complex patterns hidden in the most diverse data sources, showing robustness against noise, and receptiveness to generalization. While in the past ML has been mostly applied to data science, it has recently been used to address questions in the physical sciences. Applications to quantum many-body systems have been put forward last year, to classify phases of matter^{3–6}, and to improve the simulation of classical^{7,8} and quantum⁹ systems.

QST is by itself a data-driven problem, in which we aim to obtain a complete quantum-mechanical description of a system, on the basis of a limited set of experimentally accessible measurements.¹⁰ Key quantum features, such as multi-qubit entanglement, are however challenging to probe directly in current experimental setups.¹¹ Finding an efficient method to reliably extract such information from a generic quantum device is therefore important for the development of more powerful quantum simulators. In order to efficiently perform QST, it is necessary to find a compact, and sufficiently general representation of the quantum state to be analyzed. Matrix-Product-States (MPS) is certainly the state-of-the-art tool for the tomography of low-entangled states^{12,13}, but alternative representations are urged when performing QST of highly-entangled quantum states, resulting either from deep quantum circuits or high-dimensional physical systems.

In this Letter we show how ML approaches can be used to find such representations. In particular, we argue that suitably-trained artificial neural networks (ANN) offer a natural, efficient, and general way of performing QST driven by experimental data. Our approach is demon-

strated on controlled artificial datasets, comprising measurements from several quantum states with a large number of degrees of freedom (qubits, spins, etc...), that are thus traditionally hard for QST approaches.

The ANN architecture we use in this work is based on restricted Boltzmann machine (RBM) models. RBMs feature a visible layer (describing the physical qubits) and a hidden layer of stochastic binary neurons fully connected with weighted edges to the visible layer. These models have been successfully employed to effectively solve complex many-body problems.^{9,14,15} “Neural quantum state” representations of the many-body wavefunction have been shown to be capable of sustaining high entanglement, and to efficiently describe complex topological phases of matter.^{4,16–20} Given these favorable properties, RBM-based quantum states are natural candidates for QST of low and high-dimensional many-body systems.

Let us consider, given some reference basis \mathbf{x} (e.g. σ^z for spin- $\frac{1}{2}$), a generic many body target wave-function $\Psi(\mathbf{x}) \equiv \langle \mathbf{x} | \Psi \rangle$ describing the physical system of interest. We introduce then an RBM wave-function:

$$\psi_{\lambda,\mu}(\mathbf{x}) = \sqrt{\frac{p_{\lambda}(\mathbf{x})}{Z_{\lambda}}} e^{i\phi_{\mu}(\mathbf{x})/2} \quad (1)$$

where Z_{λ} is the normalization constant, $\phi_{\mu} = \log p_{\mu}(\mathbf{x})$ and $p_{\lambda/\mu}(\mathbf{x})$ are RBM probability distributions corresponding to two different sets λ/μ of network parameters (see Suppl. Inf.). Our ML approach to QST is then carried out as follows. First, the RBM is trained on a dataset consisting of a series of independent density measurements $|\Psi(\mathbf{x}^{[b]})|^2$ realized in a collection of bases $\{\mathbf{x}^{[b]}\}$ of the N -body quantum system. During this stage, the network parameters (λ, μ) are optimized to maximize the dataset likelihood, in a way

that $|\psi_{\lambda,\mu}(\mathbf{x}^{[b]})|^2 \simeq |\Psi(\mathbf{x}^{[b]})|^2$ (see Suppl. Inf.). Once trained, $\psi_{\lambda,\mu}(\mathbf{x})$ approximates both the wave-function's amplitudes and phases, thus reconstructing the target state. The accuracy of the reconstruction can be systematically improved by increasing the number of hidden neurons M in the RBM for fixed N , or equivalently the density of hidden units $\alpha = M/N$.⁹ One key feature of our QST approach, is that it only needs raw data, i.e. many experimental snapshots coming from single measurements, rather than estimates of expectation values of operators.^{10,12,13,21–24} This setup implies that we circumvent the need to achieve low levels of intrinsic Gaussian noise in the evaluations of mean values of operators.

To demonstrate the power of this approach, we start by considering QST of the W state, a paradigmatic N -qubit multipartite entangled wave-function defined as

$$|\Psi_W\rangle = \frac{1}{\sqrt{N}}(|100\dots\rangle + \dots + |\dots001\rangle). \quad (2)$$

To mimic experiments, we generate several datasets with an increasing number of synthetic density measurements obtained by sampling from the W state in the σ^z basis. These measurements are used to train an RBM model featuring only the set of parameters λ , since the target $|\Psi_W\rangle$ is real and positive in this basis. After the training, we sample from $|\psi_{\lambda}(\sigma^z)|^2$ and build the histogram of the frequency of the components appearing in $|\Psi_W\rangle$. In Fig. 1(a) we show three histograms obtained with a different number of samples in the training dataset for $N = 20$, and for a fixed density of hidden variables $\alpha = 1$. From the histograms, we see that upon increasing the number of samples each of the N components ($|100\dots\rangle, |010\dots\rangle, \dots$) contribute equally to the wavefunction, as expected from the exact W state. To better quantify the quality of our reconstruction we then compute the overlap $O_W = |\langle\Psi_W|\psi_{\lambda}\rangle|$ of the wave-function generated by the RBM with the original W state (see Suppl. Mat.). In Fig. 1(b) O_W is shown as a function of the number of samples in the training datasets for three different values of N . For a system size substantially larger than what is currently available in experiments,²⁵ an overlap $O_W \sim 1$ can be achieved with a limited number of samples. As a comparison, for $N = 8$, full QST requires almost 10^6 measurements,²¹ whereas our approach achieves comparable accuracy with only about 100 measurements. We further consider a phase-augmented W state, where a local phase shift $\exp(i\theta(\sigma_k^z)/2)$ with random phase $\theta(\sigma_k^z)$ is applied to each qubit. QST is now carried out using the full RBM wave-function and training on $2(N-1)$ additional bases (see Suppl. Mat.). In the lower section of Fig. 1 we plot the comparison between the exact phases (c) and the phases learned by the RBM (d) for $N = 20$ qubits, showing very good agreement ($O_W = 0.997$).

We now turn to the case of more complex systems and demonstrate QST for genuine many-body problems. To mimic experimental outcomes, we generate artificial datasets sampling different quantum states of interacting

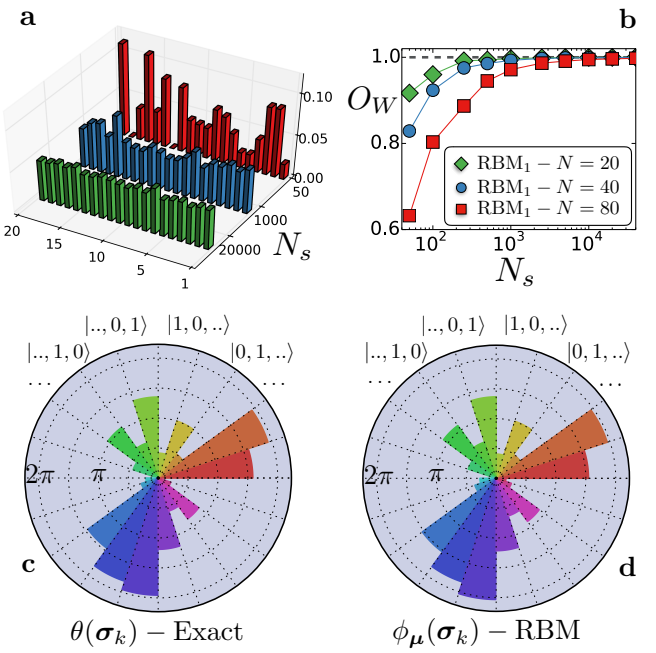


Figure 1. Tomography of the W state. **a)** Overlap between the W state and the wave-function generated by the trained RBM with $\alpha = 1$ as a function of the number of samples in the training dataset. **b)** Histogram of the occurrence of each of the superposed states in the W state for $N = 20$ qubits. We plot three histograms obtained by sampling a RBM trained on a dataset containing 50 (red), 1000 (blue) and 20000 (green) independent samples. **c-d)** Phases $\theta(\sigma_k^z)$ for each of the $N = 20$ states (different colors) in the phase augmented W state. We show the comparison between the exact phases (c) and the phases learned by a RBM (d), trained using 6400 samples per basis (magnitudes of the phases are plotted along the radial direction). RBM tomography allows here to systematically converge to the target W state for both cases with real and complex wave-function coefficients, upon increasing the number of experimental samples.

spin models on a lattice. These are directly relevant for quantum simulators based on ultra-cold ions and atoms. In particular we consider the transverse-field Ising model (TFIM) with Hamiltonian

$$\mathcal{H} = \sum_{ij} J_{ij} \sigma_i^z \sigma_j^z - h \sum_i \sigma_i^x \quad (3)$$

and the XXZ spin- $\frac{1}{2}$ model, with Hamiltonian

$$\mathcal{H} = \sum_{ij} \left[\Delta (\sigma_i^x \sigma_j^x + \sigma_i^y \sigma_j^y) + \sigma_i^z \sigma_j^z \right] \quad (4)$$

where the σ_i are Pauli spin operators.

We first discuss QST for ground state wave-functions of Hamiltonians with nearest neighbors couplings, considering both a 1-dimensional (1d) chain with N sites and a 2-dimensional (2d) square lattice with linear extent L (for a total of $N = L^2$ spins). Synthetic measurements in this case are obtained with standard quantum

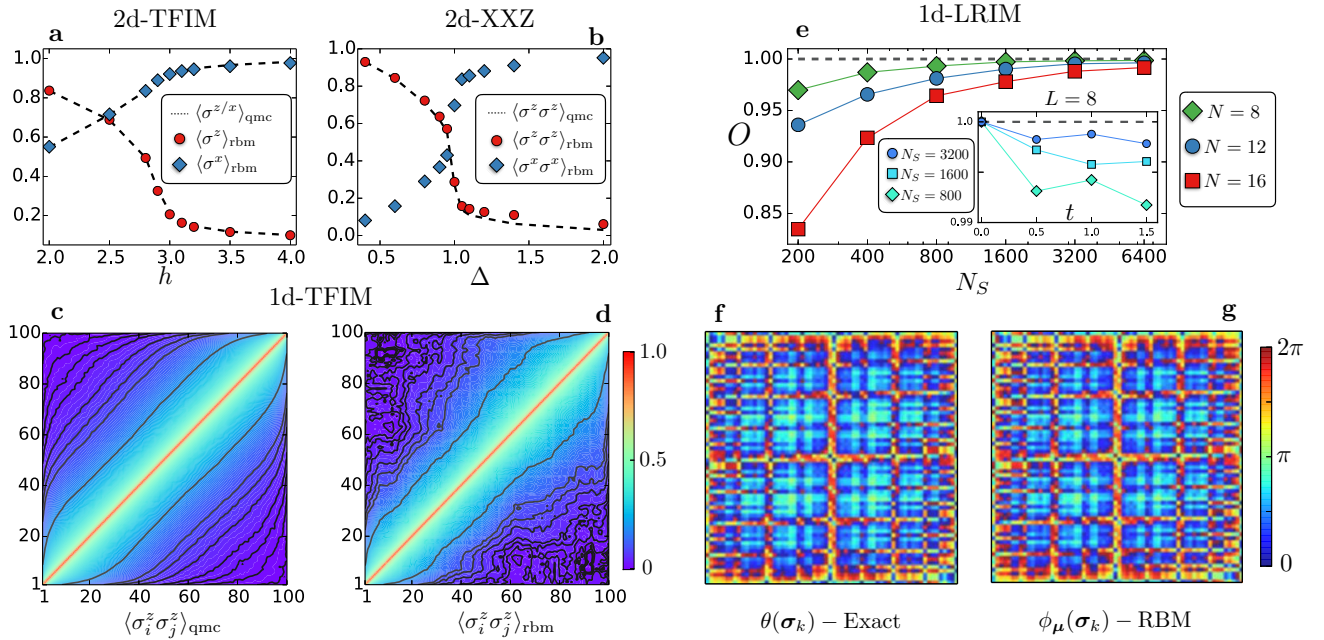


Figure 2. Tomography for many-body Hamiltonians. In panels (a-d) we show QST for ground states, comparing the reconstructed observables to those obtained with quantum Monte Carlo simulations. In panels (e-g) we show QST for unitary evolution of a 1d chain following a quantum quench with long-range Ising Hamiltonian with $\gamma = 3/4$. **a)** Diagonal and off-diagonal magnetizations as a function of the transverse field h for the ferromagnetic 2d-TFIM on a square lattice with linear size $L = 12$ ($N = 144$). **b)** Two-point correlation function (diagonal and off-diagonal) between neighboring spins along the diagonal of the square lattice (linear size $L = 12$) for the 2d-XXZ model. Each data point is obtained with a RBM from a network trained with $\alpha = 1/4$ on separate datasets. RBM-QST allows here to accurately reconstruct, for each model, both diagonal and off-diagonal observables of the target state. In the lower panels we show the reconstruction of the diagonal spin correlation function $\langle \sigma_i^z \sigma_j^z \rangle$ for the 1d-TFIM with $N = 100$ sites at the critical point $h = 1$. **c)** Direct calculation on spin configurations from a test-set much larger than the training dataset, **d)** Reconstruction of the correlations by sampling the trained RBM with $\alpha = 1/2$. **e)** Overlap between the system wave-function $\Psi(\sigma; t)$ and the RBM wave-function $\psi_{\lambda, \mu}(\sigma)$ for $t = 0.5$, as a function of the number of samples N_S per basis. In the inset we show the overlap as a function of time for different values of N_S . In the lower panels we show the reconstruction of the 2^N phases (re-arranged as a 2d array) for $N = 12$ and $t = 0.5$. **f)** Exact phases $\theta(\sigma_k)$ for each component $\Psi(\sigma_k; t)$. **g)** Phases $\phi_\mu(\sigma_k)$ learned by the RBM with $\alpha = 1$.

Monte Carlo (QMC) methods (see Supp. Inf.), stochastically sampling the exact ground-state of Hamiltonians in Eqs. (3,4) for different values of the coupling parameters h and Δ , covering the critical part of the phase diagram. The many-body ground-state wave-function is real and positive, thus our reconstruction scheme does not require measurements in any additional basis other than σ^z . Once the training is complete, we can test the representational power of the neural networks by computing various observables using the RBM and comparing with the values obtained through QMC simulations.¹⁴ In particular we consider few-body magnetic observables, such as magnetization and spin correlations.

For the TFIM we look both at the longitudinal σ^z , and transverse σ^x magnetizations. As shown in Fig. 2 (a) for $d = 2$, the RBMs can reproduce the average values with high accuracy, both for diagonal and off-diagonal observables. For the XXZ model, we show in Fig. 2 (b) for $d = 2$ the expectation values of the diagonal $\sigma_a^z \sigma_b^z$ and off-diagonal $\sigma_a^x \sigma_b^x$ spin correlations, with a and b being neighbors along the lattice diagonal. Finally, we

consider the full spin-spin $\sigma_i^z \sigma_j^z$ correlation function for the 1d-TFIM, which involves non-local correlations. We show the reconstruction of the correlation function using the RBM (Fig. 2 (d)) closely matching the exact result obtained by direct computation from the spin states on a much larger independent set of QMC measurements (Fig. 2 (c)), with deviations compatible with statistical uncertainty due to the finiteness of the training set.

In the context of many-body Hamiltonians, we now go beyond ground states and realize QST for states originating from dynamics under unitary evolution. In particular, we consider a 1d chain of Ising spins initially prepared in the state $\Psi_0 = |\rightarrow, \rightarrow, \dots, \rightarrow\rangle$ (fully aligned in the σ^x basis), subject to unitary dynamics enforced by the Hamiltonian in Eq. 3 with long-range interactions $J_{ij} \propto 1/|i - j|^\gamma$ and magnetic field set to zero ($h = 0$). This kind of “quench” dynamics is realizable in experiments with ultra-cold ions²⁶. For a given time t , we perform QST on the state $|\Psi(t)\rangle = \exp(-i\mathcal{H}t)|\Psi_0\rangle$ by training the RBM on spin density measurements performed in $2N + 1$ different basis (see Supp. Inf.). In

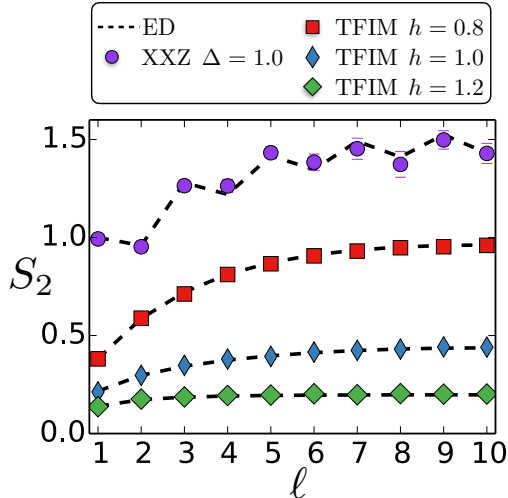


Figure 3. Reconstruction of the entanglement entropy. Second Renyi entropy as a function of the subsystem size ℓ for $N = 20$ spins. We compare results obtained using the RBM wave-functions (markers) with exact diagonalization (dashed lines) for the 1d-TFIM at different values of the transverse magnetic field h and the 1d-XXZ model with critical anisotropy $\Delta = 1$.

Fig. 2 (e) we show the overlap between the RBM wavefunction $\psi_{\lambda,\mu}(\sigma)$ and the time-evolved state $\Psi(\sigma; t)$ for different system sizes N , as a function of the number N_S of samples per basis (inset shows overlap scaling with time). In the lower plot we show for $N = 12$ the exact (f) and the reconstructed phases (g). The quality of the RBM-QST is once more remarkable, with a limited number of measurements needed.

To further assess the capabilities of our approach, we finally turn to the entanglement entropy, a highly non-local quantity particularly challenging for direct experimental observations.¹¹ It provides important information on the universal behavior of interacting many-body systems and it is of central interest in condensed matter physics and quantum information theory. Following the method proposed here, we can obtain an estimate of this quantity given only simple measurements of the density, which are more accessible with current experimental advances.²⁷ Given a bipartition of the physical system, we consider in particular the second Renyi entropy defined as $S_2(\rho_A) = -\log(\text{Tr}(\rho_A^2))$, with the subsystem ρ_A of varying size. We estimate S_2 by employing an improved ratio trick sampling²⁸ using the wave-function generated by the RBM. In Fig. 3 we show the entanglement entropy for the 1d-TFIM with three values of the transverse field, and for the critical ($\Delta = 1$) 1d-XXZ model. In both instances we took a chain with $N = 20$ spins and plot the entanglement entropy as a function of the subsystem size $\ell \in [1, N/2]$. The values obtained with the RBM (markers) are compared with results from exact diagonalization (dashed lines), with an overall good

agreement.

To conclude, we have demonstrated that ML tools can be efficiently used to reconstruct complex many-body quantum states from a limited number of experimental measurements. Our scheme is general enough to be efficiently applied to a variety of quantum devices for which current approaches demand exponentially large resources. These include QST of highly-entangled quantum circuits, adiabatic quantum simulators,²⁹ experiments with ultra-cold atoms and ions traps in higher dimensions.^{30–32} Our approach can be used to directly validate quantum computers and simulators, as well as to indirectly reconstruct quantities which are experimentally challenging for a direct observation. For example, we anticipate that the current generation of quantum microscopes could substantially benefit from neural-quantum states QST. In particular, we predict that the use of our approach for bosonic ultra-cold atoms experiments would allow for the determination of the entanglement entropy on systems substantially larger than those currently accessible with quantum interference techniques.¹¹

Acknowledgements

We thank H. Carteret and B. Kulchytskyy for useful discussions. GT thanks the Institute for Theoretical Physics, ETH Zurich, for hospitality during various stages of this work. GT and RGM acknowledge support from NSERC, the Canada Research Chair program, the Ontario Trillium Foundation, and the Perimeter Institute for Theoretical Physics. Research at Perimeter Institute is supported through Industry Canada and by the Province of Ontario through the Ministry of Research & Innovation. GC, GM and MT acknowledge support from the European Research Council through ERC Advanced Grant SIMCOFE, and the Swiss National Science Foundation through NCCR QSIT. Simulations were performed on resources provided by SHARCNET, and by the Swiss National Supercomputing Centre CSCS.

Appendix A: RBM Quantum State Tomography

We provide in this section a description of the different steps required to perform quantum state tomography (QST) with neural networks for many-body quantum systems. We concentrate on the case of systems with two local degrees of freedom (spin- $\frac{1}{2}$, qubits, etc) and choose $\sigma \equiv \sigma^z$ as the reference basis for the N -body wave-function $\Psi(\sigma) \equiv \langle \sigma | \Psi \rangle$ we intend to reconstruct. This high-dimensional function can be well approximated with an artificial neural network (NN). Given a set of input variables (for example $\sigma = \sigma_1, \sigma_2, \dots, \sigma_N$), a NN is a highly non-linear function whose output is determined by some internal parameters κ . The architecture of the network consists of a collection of elementary units, called neurons, connected by weighted edges. The strength of these connections, specified by the parameters κ , encode conditional dependence among neurons, in turn leading to complex correlations among the input variables. Increasing the number of auxiliary neurons systematically improves the expressive power of the NN function, which can then be used as a general-purpose approximator for the target wave-function.⁹ Goal of our scheme, is to find the best NN approximation for the many-body wave-function, $\psi_\kappa(\sigma)$, using only experimentally accessible information.

The QST scheme proposed proceeds as follows. First, we assume that a set of experimental measurements in a collection of bases $b = 0, 1, 2 \dots N_B$ is available. These measurements are distributed according to the probabilities $P_b(\sigma^{[b]}) \propto |\Psi(\sigma^{[b]})|^2$, thus contain information about both the amplitudes and the phases of the wave-function in the reference basis σ . Goal of the NN training, is to find the optimal set of parameters κ such that $\psi_\kappa(\sigma)$ mimics as closely as possible the data distribution in each basis, i.e. $|\psi_\kappa(\sigma^{[b]})|^2 \simeq P_b(\sigma^{[b]})$. This is achieved by searching for the NN parameters that minimize the total statistical divergence $\Xi(\kappa)$ between the target distributions and the reconstructed ones. Several possible choices can be made for $\Xi(\kappa)$. Here, we define it as the sum of the Kullbach-Leibler (KL) divergences in each basis:

$$\Xi(\kappa) \equiv \sum_{b=0}^{N_B} \mathbb{KL}_\kappa^{[b]} = \sum_{b=0}^{N_B} \sum_{\{\sigma^{[b]}\}} P_b(\sigma^{[b]}) \log \frac{P_b(\sigma^{[b]})}{|\psi_\kappa(\sigma^{[b]})|^2}. \quad (\text{A1})$$

The total divergence $\Xi(\kappa)$ is positive definite, and attains the minimum value of 0 when the reconstruction is perfect in each basis: $|\psi_\kappa(\sigma^{[b]})|^2 = P_b(\sigma^{[b]})$. Depending on the target wave-function, a sufficiently large set of measurement bases must be included, in order to have enough information to estimate the phases in the reference basis. In practice, for most states of interest it is enough to include a number of bases which scales only polynomially with system size.

Once the training is complete, the NN provides a compact representation $\psi_\kappa(\sigma)$ of the target wave-function $\Psi(\sigma)$. In turn, this representation can be used to efficiently compute various observables of interest, overlaps with other known quantum states and virtually any other information not directly accessible in the experiment. In the next two sub-sections we describe in details the specific parametrization of the NN wave-function adopted in this work and its optimization.

1. The RBM wave-function

There are many possible architecture and NN that can be employed to represent a quantum many-body state. We decide to employ a powerful stochastic NN called a restricted Boltzmann machine (RBM). The network architecture of a RBM features two layers of stochastic binary neurons, a visible layer σ describing the physical variables and a hidden layer h . The expressive power of the model can be characterized by the ratio $\alpha = M/N$ between the number of hidden neurons M and visible neurons N . A RBM is also an energy-based model, sharing many properties of physical model in statistical mechanics. In particular, it associates to the graph structure a probability distribution given by the Boltzmann distribution

$$p_\kappa(\sigma, h) = \frac{1}{Z_\kappa} e^{\sum_{ij} W_{ij}^\kappa h_i \sigma_j + \sum_j b_j^\kappa \sigma_j + \sum_i c_i^\kappa h_i}, \quad (\text{A2})$$

where $Z_\kappa = \sum_{\sigma, h} p_\kappa(\sigma, h)$ is the normalization constant and κ now consists on the weights W^κ connecting the two layers and the fields (biases) b^κ and c^κ coupled to each visible and hidden neurons, respectively. The distribution (of interest) over the visible layer is obtained by marginalization over the hidden degrees of freedom

$$p_\kappa(\sigma) = \sum_{\{h\}} p_\kappa(\sigma, h) = e^{\sum_j b_j^\kappa \sigma_j + \sum_i \log(1 + e^{c_i^\kappa + \sum_j W_{ij}^\kappa \sigma_j})}. \quad (\text{A3})$$

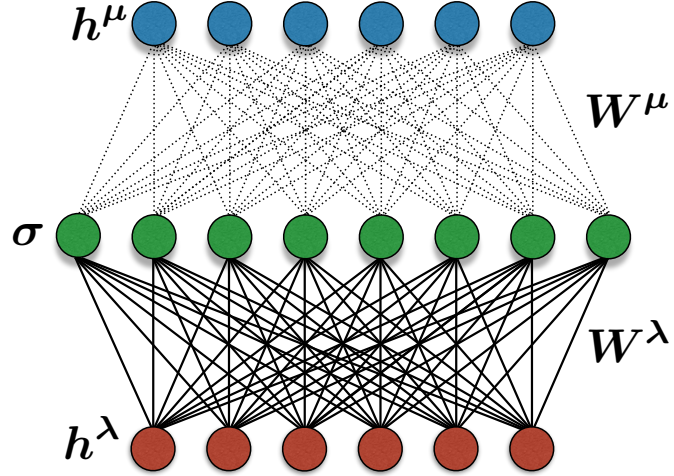


Figure 4. RBM parametrization of the wave-function: a layer σ of neurons describing the physical variables (e.g. spins, particles, etc) is connected to two hidden layers h^λ and h^μ with weights W^λ and W^μ (external fields are not drawn in the figure). Thick lines refer to the weighted connections employed in the sampling of configurations σ , while dotted lines are used to parametrize the phase ϕ_μ .

The RBM wave-function is then defined as

$$\psi_{\lambda,\mu}(\sigma) = \sqrt{\frac{p_\lambda(\sigma)}{Z_\lambda}} e^{i\phi_\mu(\sigma)/2}, \quad (\text{A4})$$

where $\phi_\mu(\sigma) = \log p_\mu(\sigma)$ and λ, μ are the two set of parameters (Fig. 4). Note that the sampling of configurations σ from $|\psi_{\lambda,\mu}(\sigma)|^2$, involves only the amplitude distribution $p_\lambda(\sigma)/Z_\lambda$. This can be achieved, as usual for RBMs, by performing Block Gibbs sampling with the two conditional distributions $p_\lambda(\sigma | h)$ and $p_\lambda(h | \sigma)$, which can be computed exactly. This procedure is very efficient since each neuron in one layer of the RBM is connected only to neurons of a different layer, thus enabling us to sample all units (in one layer) simultaneously.

2. Gradients of the total divergence

The first step in the RBMs trainings is to build the dataset of measurements. In general, different basis are needed to estimate both amplitudes and phases of the target state $\Psi(\sigma)$. We define a series of datasets D_b for each base $b = 1, \dots, N_B$, with each dataset $D_b = \{\sigma_i^{[b]}\}_{i=1}^{|D_b|}$ consisting of $|D_b|$ density measurements with underlying distribution $P_b(\sigma^{[b]}) \propto |\Psi(\sigma^{[b]})|^2$, where $\sigma^{[b]} = (\sigma_1^{[b]}, \dots, \sigma_N^{[b]})$ and $\sigma^{[0]} = \sigma$. The quantity to minimize, also called negative log-likelihood, is then

$$\Xi(\kappa) = - \sum_{b=0}^{N_B} \frac{1}{|D_b|} \sum_{\sigma^{[b]} \in D_b} \log |\psi_{\lambda,\mu}(\sigma^{[b]})|^2 \quad (\text{A5})$$

where we omitted here a constant term given by the sum of the cross-entropies of the datasets $\sum_b \mathbb{H}(D_b)$. The NN wave-function in the $\sigma^{[b]}$ bases is simply obtained by

$$\psi_{\lambda,\mu}(\sigma^{[b]}) = \sum_{\{\sigma\}} U_b(\sigma, \sigma^{[b]}) \psi_{\lambda,\mu}(\sigma), \quad (\text{A6})$$

with $U_b(\sigma, \sigma^{[b]})$ being the basis transformation matrix. The rotated state, $\psi_{\lambda,\mu}(\sigma^{[b]})$, can be computed efficiently, provided that U acts non-trivially on a limited number of qubits.

We proceed now to give the expressions for the various gradients needed in the training. By plugging Eq. A4 in Eq. A5 we obtain

$$\Xi(\lambda, \mu) = (N_B + 1) \log Z_\lambda - \sum_{b=0}^{N_B} \frac{1}{|D_b|} \sum_{\sigma^{[b]} \in D_b} \left[\log \left(\sum_{\{\sigma\}} U_b(\sigma, \sigma^{[b]}) \sqrt{p_\lambda(\sigma)} e^{i\phi_\mu(\sigma)/2} \right) + c.c. \right]. \quad (\text{A7})$$

We define now the two gradients

$$\mathcal{D}_{\lambda}(\boldsymbol{\sigma}) = \frac{1}{p_{\lambda}(\boldsymbol{\sigma})} \nabla_{\lambda} p_{\lambda}(\boldsymbol{\sigma}) \quad (\text{A8})$$

$$\mathcal{D}_{\mu}(\boldsymbol{\sigma}) = \nabla_{\mu} \phi_{\mu}(\boldsymbol{\sigma}), \quad (\text{A9})$$

where the derivatives of the RBM distribution are:

$$\frac{\partial}{\partial W_{ij}} p_{\kappa}(\boldsymbol{\sigma}) = \frac{\sigma_j}{1 + e^{-\sum_j W_{ij}^{\kappa} \sigma_j - c_i}}, \quad (\text{A10})$$

$$\frac{\partial}{\partial b_j} p_{\kappa}(\boldsymbol{\sigma}) = \sigma_j, \quad (\text{A11})$$

and

$$\frac{\partial}{\partial c_i} p_{\kappa}(\boldsymbol{\sigma}) = \frac{1}{1 + e^{-\sum_j W_{ij}^{\kappa} \sigma_j - c_i}}. \quad (\text{A12})$$

We also define the quasi-probability distribution

$$Q_b(\boldsymbol{\sigma}, \boldsymbol{\sigma}^{[b]}) = U_b(\boldsymbol{\sigma}, \boldsymbol{\sigma}^{[b]}) \sqrt{p_{\lambda}(\boldsymbol{\sigma})} e^{i\phi_{\mu}(\boldsymbol{\sigma})/2}. \quad (\text{A13})$$

Then, the derivatives of the KL divergence with respect to the parameters λ and μ are

$$\nabla_{\lambda} \Xi(\lambda, \mu) = (N_B + 1) \langle \mathcal{D}_{\lambda} \rangle_{p_{\lambda}} - \sum_{b=0}^{N_B} \frac{1}{|D_b|} \sum_{\boldsymbol{\sigma}^{[b]} \in D_b} \text{Re} \{ \langle \mathcal{D}_{\lambda} \rangle_{Q_b} \}, \quad (\text{A14})$$

and

$$\nabla_{\mu} \Xi(\lambda, \mu) = \sum_{b=0}^{N_B} \frac{1}{|D_b|} \sum_{\boldsymbol{\sigma}^{[b]} \in D_b} \text{Im} \{ \langle \mathcal{D}_{\mu} \rangle_{Q_b} \}. \quad (\text{A15})$$

In the expression above we have defined the pseudo-averages:

$$\langle \mathcal{D}_{\lambda/\mu} \rangle_{Q_b} = \frac{\sum_{\{\boldsymbol{\sigma}\}} \mathcal{D}_{\lambda/\mu}(\boldsymbol{\sigma}) Q_b(\boldsymbol{\sigma}, \boldsymbol{\sigma}^{[b]}) \psi_{\lambda, \mu}(\boldsymbol{\sigma})}{\sum_{\{\boldsymbol{\sigma}\}} Q_b(\boldsymbol{\sigma}, \boldsymbol{\sigma}^{[b]}) \psi_{\lambda, \mu}(\boldsymbol{\sigma})}, \quad (\text{A16})$$

which can be efficiently computed directly summing over the samples in the datasets D_b . On the other hand, the evaluation of the average

$$\langle \mathcal{D}_{\lambda} \rangle_{p_{\lambda}} = \frac{1}{Z_{\lambda}} \sum_{\{\boldsymbol{\sigma}\}} p_{\lambda}(\boldsymbol{\sigma}) \mathcal{D}_{\lambda}(\boldsymbol{\sigma}), \quad (\text{A17})$$

requires the knowledge of the normalization constant Z_{λ} , which is not directly accessible. However, as per standard RBM training,³³ one can approximate this average by

$$\langle \mathcal{D}_{\lambda} \rangle_{p_{\lambda}} \simeq \frac{1}{n} \sum_{k=1}^n \mathcal{D}_{\lambda}(\boldsymbol{\sigma}_k), \quad (\text{A18})$$

where $\boldsymbol{\sigma}_k$ are samples generated using a Markov-chain Monte Carlo simulation.

Finally, we point out that in our work we have adopted a slightly simplified training scheme. In particular, we break down the training into two steps. First, we learn the amplitudes only by optimizing the parameters λ . In this case, it is sufficient to minimize the KL divergence over the reference basis only (i.e. $\boldsymbol{\sigma}$). This part of the training is to all purposes a standard unsupervised learning procedure, involving the generation of samples from the RBM.³⁴ Then, we fix the parameters λ , and use the measurements in the auxiliary bases to determine the optimal values of the phase parameters μ . This other part of the training is achieved using the gradient in Eq. A15, thus not requiring Monte Carlo sampling from the NN.

3. Training the neural network

For a given set of parameters (e.g. μ), the easiest way to numerically minimize the total divergence, Eq. A5, is by using simple stochastic gradient descent³⁴. Each parameter μ_j is updated as

$$\mu_j \leftarrow \mu_j - \eta \langle g_j \rangle_B, \quad (\text{A19})$$

where the gradient step η is called learning rate and the gradient g_j is averaged over a batch B ($|B| \ll |D|$) of samples drawn randomly from the full dataset:

$$\langle g_j \rangle_B = \frac{1}{|B|} \sum_{\sigma \in B} \text{Im} \{ \langle \mathcal{D}_{\mu_j} \rangle_{Q_b} \}. \quad (\text{A20})$$

Stochastic gradient descent was the optimization method used to learn the amplitudes of each physical system presented in the paper. For the learning of the phases however, we instead implemented the natural gradient descent³⁵, which revealed to be more effective, though at the cost of increased computational resources. In this case we update the parameters as

$$\mu_j \leftarrow \mu_j - \eta \sum_i \langle S_{ij}^{-1} \rangle_B \langle g_j \rangle_B, \quad (\text{A21})$$

where we have introduced the Fisher information matrix:

$$\langle S_{ij} \rangle_B = \frac{1}{|B|} \sum_{\sigma \in B} \text{Im} \{ \langle \mathcal{D}_{\mu_i} \rangle_{Q_b} \} \text{Im} \{ \langle \mathcal{D}_{\mu_j} \rangle_{Q_b} \}. \quad (\text{A22})$$

The learning rate magnitude η is set to

$$\eta = \frac{\eta_0}{\sqrt{\sum_{ij} \langle S_{ij} \rangle_B \times \langle g_i \rangle_B \langle g_j \rangle_B}} \quad (\text{A23})$$

with some initial learning rate η_0 . The matrix $\langle S_{ij} \rangle_B$ takes into account the fact that, since the parametric dependence of the RBM function is non-linear, a small change of some parameters may correspond to a very large change of the distribution. In this way one implicitly uses an adaptive learning rate for each parameter μ_j and speed-up the optimization compared to the simplest gradient descent. We notice that a very similar technique is successfully used in Quantum Monte Carlo for optimizing high-dimensional variational wave-functions³⁶. Similarly to our case, noisy gradients, which come from the Monte Carlo statistical evaluation of energy derivatives with respect to the parameters, are present, while the matrix S is instead given by the covariance matrix of these forces. Since the matrix $\langle S_{ij} \rangle_B$ is affected by statistical noise, we regularize it by adding a small diagonal offset, thus improving the stability of the optimization.

4. Training datasets

In our work we have benchmarked NN-QST on artificial datasets, consisting of a collection of independent measurements obtained by projecting the physical system wave-function $|\Psi\rangle$ into the various basis $\{\sigma^{[b]}\}$. Whenever possible, we perform exact sampling of the full wave-function $\Psi(\sigma)$, that is when the system size is small enough, or the wave-function itself is simple enough (e.g. W state). In the case of QST for ground states of local Hamiltonian, we investigated system sizes out of the reach of any exact diagonalization techniques, and we therefore build the datasets using quantum Monte Carlo (QMC) simulations.

We use the Path-Integral Monte Carlo (PIMC) variant of the QMC family of algorithms, which allows us to sample from the exact ground state density distribution $|\Psi(\sigma)|^2$ for the Transverse field Ising model (TFIM) and the anisotropic Heisenberg model (XXZ), whose Hamiltonians \mathcal{H} are defined in the main text. The PIMC method relies on the property that the partition functions of these d -dimensional quantum spin- $\frac{1}{2}$ systems can be mapped onto that of $(d+1)$ -dimensional classical systems.³⁷ The additional dimension is called "imaginary time" τ , which goes from 0 to $\beta = 1/T$, i.e. the inverse physical temperature of the model. In this work we employ the discrete-time version of the PIMC algorithm, where the total "imaginary time" β is discretized in M_τ steps, and the simulations are exact in the $\beta/M_\tau \rightarrow 0$ limit. Therefore the quantum simulations of the N spins TFIM is mapped onto a system of $N \times M_\tau$ classical spin variables, with suitable interactions along the "imaginary time" direction (see Ref. 37 for details).

Classical Metropolis Monte Carlo (MC) on this larger system can then be performed in order to collect samples of the quantum distribution in the $\{\sigma\}$ basis. Since we are interested in the ground state distribution, we use a sufficiently large inverse temperature, in the range $\beta = 10 - 20$ and a converged number of $M_\tau = 1024 - 2048$. Statistically independent samples are collected during each MC simulation waiting for a sufficiently large number of MC moves, i.e. larger than the autocorrelation time of the Markov chain. In order to decrease the autocorrelations between successive MC configurations we use cluster update algorithms. In the case of the TFIM we use the Wolff single cluster algorithm³⁸. Here clusters can be un-restricted in the volume or restricted in such a way to extend only along the "imaginary time" direction^{39,40}. Both choices drastically improve the efficiency compared to the simple local update scheme. For the XXZ model we use a single cluster update version of the Loop algorithm⁴¹.

Appendix B: Cases of Study

We now describe the details concerning trainings and the measurements for the physical systems investigated in the main paper.

1. W state

The N -qubits W state

$$|\Psi_W\rangle = \frac{1}{\sqrt{N}} \left(|100\dots\rangle + |010\dots\rangle + \dots + |0\dots01\rangle \right), \quad (\text{B1})$$

can be efficiently sampled to generate the training datasets, irrespectively on the system size N . Moreover, since each coefficient $\Psi_W(\sigma)$ is real and positive, we only need to learn the amplitudes and we can adopt the reduced a simpler version of the RBM wave-function, that is

$$\psi_{\lambda}(\sigma) = \sqrt{\frac{p_{\lambda}(\sigma)}{Z_{\lambda}}}, \quad (\text{B2})$$

thus using only one set (λ) of network parameters.

To quantify the performances of the training we compute the overlap O between the W state wave-function and the RBM wave-function

$$O = \langle \Psi_W | \psi_{\lambda} \rangle = \sum_{\sigma} \Psi_W(\sigma) \psi_{\lambda}(\sigma), \quad (\text{B3})$$

where $\Psi_W(\sigma) = \delta(\sigma - 2^k)/\sqrt{N}$ for $k \in (0, \dots, N-1)$. As we cannot perform the full sum in Eq. B3 for large system sizes N , and we do not know the normalization constant Z_{λ} , we instead compute the square of the overlap as

$$\begin{aligned} O^2 &= \frac{\langle \Psi_W | \psi_{\lambda} \rangle}{\langle \psi_{\lambda} | \psi_{\lambda} \rangle} \times \frac{\langle \Psi_W | \psi_{\lambda} \rangle}{\langle \Psi_W | \Psi_W \rangle} \\ &= \frac{\sum_{\sigma} |\psi_{\lambda}(\sigma)|^2 \frac{\Psi_W(\sigma)}{\psi_{\lambda}(\sigma)}}{\sum_{\sigma} |\psi_{\lambda}(\sigma)|^2} \times \frac{\sum_{\sigma} |\Psi_W(\sigma)|^2 \frac{\psi_{\lambda}(\sigma)}{\Psi_W(\sigma)}}{\sum_{\sigma} |\Psi_W(\sigma)|^2} \\ &= \left\langle \frac{\Psi_W(\sigma)}{\sqrt{p_{\lambda}(\sigma)}} \right\rangle_{p_{\lambda}} \times \left\langle \frac{\sqrt{p_{\lambda}(\sigma)}}{\Psi_W(\sigma)} \right\rangle_{|\Psi_W|^2} \\ &= \left(\frac{1}{n} \sum_{j=1}^n \frac{1}{\sqrt{p_{\lambda}(\sigma_j)}} \sum_{k=0}^{N-1} \frac{\delta(\sigma_j - 2^k)}{\sqrt{N}} \right) \times \left(\sum_{k=0}^{N-1} \sqrt{\frac{p_{\lambda}(\sigma = 2^k)}{N}} \right), \end{aligned} \quad (\text{B4})$$

where the qubits configurations σ_j are drawn directly from the trained RBM distribution $p_{\lambda}(\sigma)$ by performing block Gibbs sampling from the two conditional distributions $p_{\lambda}(\sigma | h)$ and $p_{\lambda}(h | \sigma)$.

We now consider the case where local phase shifts with random phases θ_j are applied to the W state:

$$|\tilde{\Psi}_W\rangle = \frac{1}{\sqrt{N}} \left(e^{i\theta_1} |100\dots\rangle + e^{i\theta_2} |010\dots\rangle + \dots + e^{i\theta_N} |0\dots01\rangle \right). \quad (\text{B5})$$

In this case, we use the full wave-function $\psi_{\lambda,\mu}(\sigma)$ to learn both amplitude and phases. Given the structure of the state $|\tilde{\Psi}_W\rangle$, we require the $(N - 1)$ supplementary basis

$$\{X, X, Z, Z, \dots\}, \{Z, X, X, Z, \dots\}, \{Z, Z, X, X, \dots\}, \quad (\text{B6})$$

where in the basis $\{X_j, X_{j+1}\}$ we have $|\tilde{\Psi}_W|^2 \propto \cos(\theta_{j+1} - \theta_j)$, and the $(N - 1)$ supplementary basis

$$\{X, Y, Z, Z, \dots\}, \{Z, X, Y, Z, \dots\}, \{Z, Z, X, Y, \dots\}, \quad (\text{B7})$$

where in the basis $\{X_j, Y_{j+1}\}$ we have $|\tilde{\Psi}_W|^2 \propto \sin(\theta_{j+1} - \theta_j)$. The RBM is then trained on a total of $2N - 1$ basis (including the standard basis for the amplitude learning). The transformation matrices for the j -th basis ($\{X_j, X_{j+1}\}$) and ($\{X_j, Y_{j+1}\}$) are given by $U_j^{XX} = H_j \otimes H_{j+1}$ and $U_j^{XY} = H_j \otimes K_{j+1}$ respectively, where

$$H = \frac{1}{\sqrt{2}} \begin{bmatrix} 1 & 1 \\ 1 & -1 \end{bmatrix} \quad K = \frac{1}{\sqrt{2}} \begin{bmatrix} 1 & -i \\ 1 & i \end{bmatrix}, \quad (\text{B8})$$

The average of the gradient \mathcal{D}_μ over the quasi-probability distribution $Q_j^{X\nu}$ ($\nu = X, Y$) is then given by

$$\begin{aligned} \langle \mathcal{D}_\mu \rangle_{Q_j^{X\nu}} &= \frac{\sum_\sigma U_j^{X\nu}(\sigma, \sigma^{[j]}) \mathcal{D}_\mu(\sigma) \psi_{\lambda, \mu}(\sigma)}{\sum_\sigma U_j^{X\nu}(\sigma, \sigma^{[j]}) \psi_{\lambda, \mu}(\sigma)} \\ &= \frac{1}{\Lambda^j(\sigma^{[j]})} \left[\mathcal{D}_\mu(\sigma_{00}^{[j]}) \xi_{\lambda, \mu}(\sigma_{00}^{[j]}) + i^{\delta_{\nu, X}} (1 - 2\sigma_{j+1}^\nu) \mathcal{D}_\mu(\sigma_{01}^{[j]}) \xi_{\lambda, \mu}(\sigma_{01}^{[j]}) + \right. \\ &\quad \left. + (1 - 2\sigma_j^x) \mathcal{D}_\mu(\sigma_{10}^{[j]}) \xi_{\lambda, \mu}(\sigma_{10}^{[j]}) + i^{\delta_{\nu, X}} (1 - 2\sigma_{j+1}^\nu) (1 - 2\sigma_j^x) \mathcal{D}_\mu(\sigma_{11}^{[j]}) \xi_{\lambda, \mu}(\sigma_{11}^{[j]}) \right] \end{aligned} \quad (\text{B9})$$

where we defined

$$\begin{aligned} \Lambda^j(\sigma^{[j]}) &= \xi_{\lambda, \mu}(\sigma_{00}^{[j]}) + i^{\delta_{\nu, X}} (1 - 2\sigma_{j+1}^\nu) (1 - 2\sigma_j^x) \xi_{\lambda, \mu}(\sigma_{11}^{[j]}) + \\ &\quad + i^{\delta_{\nu, X}} (1 - 2\sigma_{j+1}^\nu) \xi_{\lambda, \mu}(\sigma_{01}^{[j]}) + (1 - 2\sigma_j^x) \xi_{\lambda, \mu}(\sigma_{10}^{[j]}), \end{aligned} \quad (\text{B10})$$

$$\xi_{\lambda, \mu}(\sigma_{\alpha\beta}^{[j]}) = \left(\sum_{\alpha=0,1} \sum_{\beta=0,1} \sqrt{p_\lambda(\sigma_{\alpha\beta}^{[j]})} \right)^{-1} \sqrt{p_\lambda(\sigma_{\alpha\beta}^{[j]})} e^{i\phi_\mu(\sigma_{\alpha\beta}^{[j]})/2}, \quad (\text{B11})$$

and $\sigma_{\alpha\beta}^{[j]} = (\sigma_1^z, \dots, \sigma_j^z = \alpha, \sigma_{j+1}^z = \beta, \dots, \sigma_N^z)$.

2. Magnetic observables of local Hamiltonians

The many-body Hamiltonians considered in this work are the TFIM and the XXZ model. In both cases, the ground state wave-function is real and positive, which means we can again restrict ourselves to learn the amplitudes with one set of parameters, i.e. using the RBM wave-function $\psi_\lambda(\sigma)$. Instead of computing the overlap, which is clearly intractable for the system sizes of interest, we evaluate the quality of the QST by comparing different magnetic observables computed using the RBM wave-function, with results obtained with Quantum Monte Carlo (QMC) simulations.

Given some observable $\mathcal{O} = \sum_{\sigma, \sigma'} \mathcal{O}_{\sigma\sigma'} |\sigma\rangle\langle\sigma'|$, we can calculate its expectation value using the RBM wave-function as

$$\langle \mathcal{O} \rangle = \sum_{\sigma, \sigma'} \psi_\lambda(\sigma) \psi_\lambda(\sigma') \mathcal{O}_{\sigma\sigma'}. \quad (\text{B12})$$

If the operator \mathcal{O} is diagonal in the $\{\sigma\}$ basis, i.e. $\mathcal{O}_{\sigma\sigma'}^D = \mathcal{O}(\sigma) \delta_{\sigma\sigma'}$, then

$$\begin{aligned} \langle \mathcal{O}^D \rangle &= \sum_{\sigma} |\psi_\lambda(\sigma)|^2 \mathcal{O}(\sigma) = \frac{1}{Z_\lambda} \sum_{\sigma} p_\lambda(\sigma) \mathcal{O}(\sigma) \\ &\simeq \frac{1}{n} \sum_{k=1}^n \mathcal{O}(\sigma_k), \end{aligned} \quad (\text{B13})$$

where σ_k are sampled directly with the RBM. If, on the other hand, the operator \mathcal{O} is off-diagonal, we can still compute its expectation value, provided that its matrix representation in the $\{\sigma\}$ basis is sparse. In this case, we obtain

$$\langle \mathcal{O}^{ND} \rangle = \sum_{\sigma} |\psi_{\lambda}(\sigma)|^2 \mathcal{O}_L(\sigma) \simeq \frac{1}{n} \sum_{k=1}^n \mathcal{O}_L(\sigma_k), \quad (\text{B14})$$

where

$$\mathcal{O}_L(\sigma) = \sum_{\sigma'} \sqrt{\frac{p_{\lambda}(\sigma')}{p_{\lambda}(\sigma)}} \mathcal{O}_{\sigma\sigma'}, \quad (\text{B15})$$

is the so-called "local estimate" of \mathcal{O} . For the TFIM we compare the value of the off-diagonal transverse field magnetization $\langle \sigma^x \rangle = \sum_{i=1}^N \langle \sigma_i^x \rangle$, with its QMC estimate obtained following the path-integral formulation of the expectation value of non-diagonal operators (see Ref. 42 for its explicit derivation).

3. Unitary evolution

In the previous section we discussed QST of ground state wave-functions for many-body Hamiltonians. In addition to this case, we have also investigated the unitary dynamics induced by Hamiltonian evolution. We consider the quantum "quench" setting, where the physical system is prepared in a state $|\Psi_0\rangle$ and it is time evolved with an Hamiltonian \mathcal{H} , leading to the state:

$$|\Psi(t)\rangle = e^{-i\mathcal{H}t} |\Psi_0\rangle. \quad (\text{B16})$$

In this case, for some fixed time t we build a dataset of spins density measurements $P_b(\sigma, t) = |\Psi(\sigma^{[b]}, t)|^2$ and train the RBM to learn $\Psi(\sigma, t)$. Since, because of the time evolution operator, the state is complex-valued, we once again employ the full RBM wave-function $\psi_{\lambda,\mu}(\sigma)$ for the QST. In this case, the bases $\{Z, \dots, X_j, \dots, Z\}$ and $\{Z, \dots, Y_j, \dots, Z\}$, respectively with bases rotations $U_j^X = H_j$ and $U_j^Y = K_j$, are sufficient to reconstruct the wave-function phases.

The average of the gradient \mathcal{D}_{μ} over the quasi-probability distribution Q_j^{ν} ($\nu = X, Y$) is now given by:

$$\begin{aligned} \langle \mathcal{D}_{\mu} \rangle_{Q_j^{\nu}} &= \frac{\sum_{\sigma} U_j^{\nu}(\sigma, \sigma^{[j]}) \mathcal{D}_{\mu}(\sigma) \psi_{\lambda,\mu}(\sigma)}{\sum_{\sigma} U_j^{\nu}(\sigma, \sigma^{[j]}) \psi_{\lambda,\mu}(\sigma)} \\ &= \frac{\mathcal{D}_{\mu}(\sigma_0^{[j]}) + i^{\delta_{\nu,X}} (1 - 2\sigma_j^{\nu}) \mathcal{D}_{\mu}(\sigma_1^{[j]}) \xi_{\lambda,\mu}(\sigma^{[j]})}{1 + i^{\delta_{\nu,X}} (1 - 2\sigma_j^{\nu}) \xi_{\lambda,\mu}(\sigma^{[j]})}, \end{aligned} \quad (\text{B17})$$

where we have defined

$$\xi_{\lambda,\mu}(\sigma^{[j]}) = \sqrt{\frac{p_{\lambda}(\sigma_1^{[j]})}{p_{\lambda}(\sigma_0^{[j]})}} e^{i(\phi_{\mu}(\sigma_1^{[j]}) - \phi_{\mu}(\sigma_0^{[j]}))/2}, \quad (\text{B18})$$

and $\sigma_{\alpha}^{[j]} = (\sigma_1^z, \dots, \sigma_j^z = \alpha, \dots, \sigma_N^z)$.

4. Entanglement entropy

Given a bipartition of the physical system in a subregion A and its complement A^{\perp} , the (generalized) entanglement Renyi entropies are defined as

$$S_{\alpha}(\rho_A) = \frac{1}{1-\alpha} \log[\text{Tr}(\rho_A^{\alpha})], \quad (\text{B19})$$

where $\rho_A = \text{Tr}_{A^{\perp}}(\rho)$ is the reduced density matrix for subregion A. We can write the RBM wave-function (previously trained in the usual way) in the general form

$$|\psi_{\lambda}\rangle = \sum_{\alpha, \alpha^{\perp}} \Gamma_{\alpha \alpha^{\perp}}^{\lambda} |\alpha\rangle \otimes |\alpha^{\perp}\rangle, \quad (\text{B20})$$

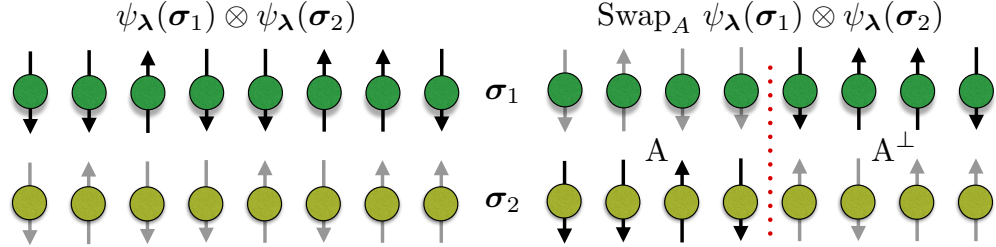


Figure 5. Replica trick for the evaluation of the second Renyi entropy.

where $\{\alpha\}$ and $\{\alpha^\perp\}$ are basis state for the subregions A and A^\perp respectively.

For simplicity, we also assume in the following that the wave-function Ψ is real and positive. We then consider two non-interacting copies of the physical system in a product state and introduce the Swap operator

$$\begin{aligned} \text{Swap}_A |\psi_{\lambda}\rangle \otimes |\psi_{\lambda}\rangle &= \text{Swap}_A \left(\sum_{\alpha_1, \alpha_1^\perp} \Gamma_{\alpha_1 \alpha_1^\perp}^\lambda |\alpha_1\rangle \otimes |\alpha_1^\perp\rangle \right) \otimes \left(\sum_{\alpha_2, \alpha_2^\perp} \Gamma_{\alpha_2 \alpha_2^\perp}^\lambda |\alpha_2\rangle \otimes |\alpha_2^\perp\rangle \right) \\ &= \sum_{\alpha_1, \alpha_1^\perp} \sum_{\alpha_2, \alpha_2^\perp} \Gamma_{\alpha_1 \alpha_1^\perp}^\lambda \Gamma_{\alpha_2 \alpha_2^\perp}^\lambda (|\alpha_1\rangle \otimes |\alpha_2^\perp\rangle) \otimes (|\alpha_2\rangle \otimes |\alpha_1^\perp\rangle). \end{aligned} \quad (\text{B21})$$

It follows that the expectation value of the Swap operator is

$$\begin{aligned} \langle \text{Swap}_A \rangle &= \sum_{\alpha_1, \alpha_1^\perp} \sum_{\alpha_2, \alpha_2^\perp} \Gamma_{\alpha_1 \alpha_1^\perp}^\lambda (\Gamma_{\alpha_2 \alpha_2^\perp}^\lambda)^* \Gamma_{\alpha_2 \alpha_2^\perp}^\lambda (\Gamma_{\alpha_2 \alpha_2^\perp}^\lambda)^* \\ &= \text{Tr}(\rho_A^2) = e^{-S_2(\rho_A)}. \end{aligned} \quad (\text{B22})$$

Although the replica trick shown above already provides a way to compute the entanglement entropy, the expectation values of the Swap operator becomes very small when the subregion size grows larger, leading to very high sampling noise. To avoid this issue, we implement the improved ratio trick, proposed in Ref. 28. Assuming we are dealing with a 1d chain with N sites, the entanglement entropy for a subregion A of n sites can be computed as

$$S_2(\rho_A) = - \sum_{j=0}^{n-1} \log \frac{\langle \text{Swap}_{A^{j+1}} \rangle}{\langle \text{Swap}_{A^j} \rangle}, \quad (\text{B23})$$

where A^j contains j sites and $\langle \text{Swap}_{A^0} \rangle = 1$. To estimate such expectation values we consider again the expansion of the composite wave-function

$$|\psi_{\lambda}\rangle \otimes |\psi_{\lambda}\rangle = \sum_{\sigma_1} \sum_{\sigma_2} \psi_{\lambda}(\sigma_1) \psi_{\lambda}(\sigma_2) |\sigma_1\rangle \otimes |\sigma_2\rangle, \quad (\text{B24})$$

on which the expectation value of the Swap operator is

$$\langle \text{Swap}_A^j \rangle = \sum_{\sigma_1} \sum_{\sigma_2} \psi_{\lambda}(\sigma_1) \psi_{\lambda}(\sigma_2) \psi_{\lambda}(\sigma_{12}^j) \psi_{\lambda}(\sigma_{21}^j), \quad (\text{B25})$$

where we defined $\sigma_{12}^j = (\sigma_1^1, \sigma_1^2, \dots, \sigma_1^{j-1}, \sigma_2^j, \dots, \sigma_2^N)$ and $\sigma_{21}^j = (\sigma_2^1, \sigma_2^2, \dots, \sigma_2^{j-1}, \sigma_1^j, \dots, \sigma_1^N)$. The ratio of expectation values then can be rewritten as

$$\begin{aligned} \frac{\langle \text{Swap}_A^{j+1} \rangle}{\langle \text{Swap}_A^j \rangle} &= \frac{\sum_{\sigma_1} \sum_{\sigma_2} \psi_{\lambda}(\sigma_1) \psi_{\lambda}(\sigma_2) \psi_{\lambda}(\sigma_{12}^{j+1}) \psi_{\lambda}(\sigma_{21}^{j+1})}{\sum_{\sigma_1} \sum_{\sigma_2} \psi_{\lambda}(\sigma_1) \psi_{\lambda}(\sigma_2) \psi_{\lambda}(\sigma_{12}^j) \psi_{\lambda}(\sigma_{21}^j)} \\ &= \frac{\sum_{\sigma_1} \sum_{\sigma_2} \psi_{\lambda}(\sigma_1) \psi_{\lambda}(\sigma_2) \psi_{\lambda}(\sigma_{12}^j) \psi_{\lambda}(\sigma_{21}^j) \frac{\psi_{\lambda}(\sigma_{12}^{j+1}) \psi_{\lambda}(\sigma_{21}^{j+1})}{\psi_{\lambda}(\sigma_{12}^j) \psi_{\lambda}(\sigma_{21}^j)}}{\sum_{\sigma_1} \sum_{\sigma_2} \psi_{\lambda}(\sigma_1) \psi_{\lambda}(\sigma_2) \psi_{\lambda}(\sigma_{12}^j) \psi_{\lambda}(\sigma_{21}^j)} \\ &= \frac{\sum_{\sigma_1} \sum_{\sigma_2} P^j(\sigma_1, \sigma_2) \mathcal{R}^j(\sigma_1, \sigma_2)}{\sum_{\sigma_1} \sum_{\sigma_2} P^j(\sigma_1, \sigma_2)} \\ &= \langle \mathcal{R}^j(\sigma_1, \sigma_2) \rangle_P, \end{aligned} \quad (\text{B26})$$

where we defined the probability distribution $P^j(\sigma_1, \sigma_2) = \psi_{\lambda}(\sigma_1)\psi_{\lambda}(\sigma_2)\psi_{\lambda}(\sigma_{12}^j)\psi_{\lambda}(\sigma_{21}^j)$ and the observable

$$\mathcal{R}^j(\sigma_1, \sigma_2) = \frac{\psi_{\lambda}(\sigma_{12}^{j+1})\psi_{\lambda}(\sigma_{21}^{j+1})}{\psi_{\lambda}(\sigma_{12}^j)\psi_{\lambda}(\sigma_{21}^j)}. \quad (\text{B27})$$

To compute the expectation value $\langle \mathcal{R}^j(\sigma_1, \sigma_2) \rangle_{P^j}$ we employ standard Monte Carlo simulation, where spin configurations (σ_1, σ_2) for the two copies are sampled from the probability distribution $P^j(\sigma_1, \sigma_2)$. To compute the entanglement entropy for a half-chain we run $N/2$ separate Markov chain for each $j = 1, \dots, N/2$ and compute the entropy as

$$S_2(\rho_{N/2}) = - \sum_{j=0}^{N/2-1} \log \langle \mathcal{R}^j(\sigma_1, \sigma_2) \rangle_{\text{mc}}. \quad (\text{B28})$$

Appendix C: Overfitting

As per all machine learning applications, the training process should be carefully designed to avoid overfitting. This issue occurs when a complex model does not generalize well to unseen data, even though the model fits well the training data. In our experiments with RBMs, overfitting may manifest itself when the model is excessively powerful, i.e. when $\alpha \gg 1$, and/or when the data sets used during the training stage are statistically small. We investigate the overfitting in the training of our RBMs applied to the W state in two ways. First, we track the overlap O between the W state wave-function and the RBM wave-function, which should approach 1 for a properly trained model. In Fig. 6(a) we present the overlap O between the W state wave-function and the RBM wave-function as a function of the size of the training data N_s for different values of α and fixed number of qubits $N = 20$. We first note that for small α the RBM states are generically poor approximations to the W state. As long as the size of the training dataset is small, increasing α is not enough to achieve a significant improvement in the overlap O . Upon increasing

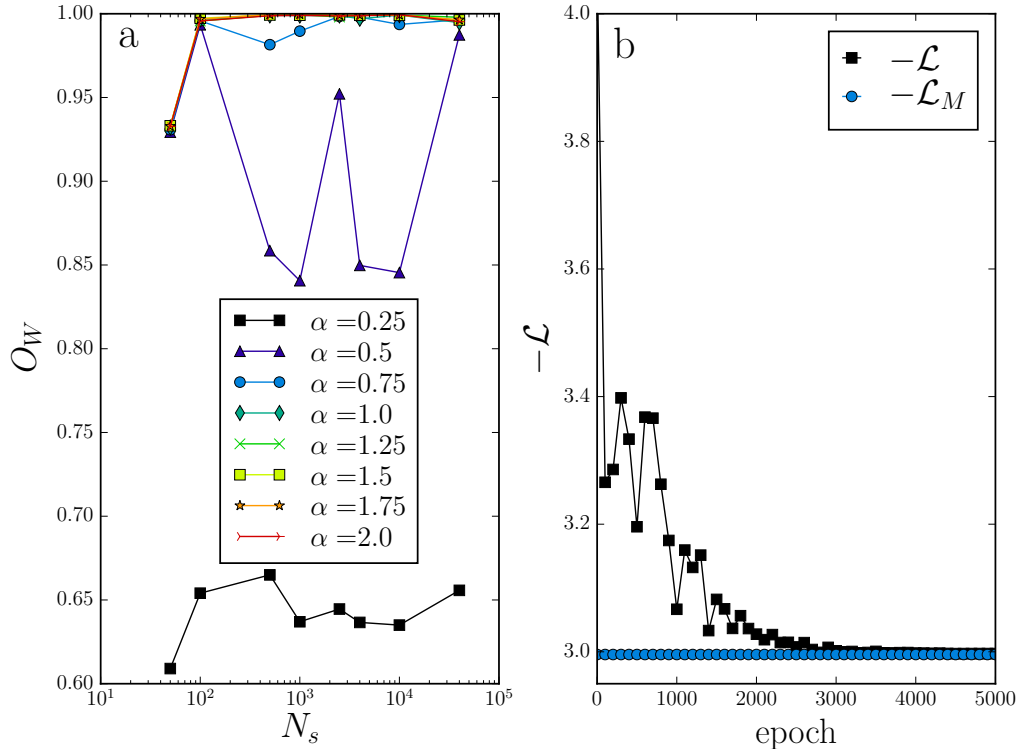


Figure 6. Investigating overfitting of RBMs in the learning of the W state. (a) The overlap O between the W state wave-function and the RBM wave-function as a function of the size of the training data N_s for different values of α and fixed value of $N = 20$. (b) The negative log-likelihood measure of a held-out test set with $N_t = 10000$ as a function of the training epoch for an RBM with $N = 20$ and $\alpha = 1$ trained on a dataset with $N_s = 40000$.

N_s , however, increasing the capacity of the RBM to $\alpha = 1$ results in overlaps approaching $O \approx 1$. Crucially, further increasing α does not deteriorate the values of O attained by the RBMs, and it rather saturates, which we attribute to having significantly large datasets that prevent overfitting. Second, we track the probability of a held-out test set during the training, which relates to the objective function that we minimize during the training. Given a dataset, the log-likelihood of the data is given by

$$\mathcal{L} = \frac{1}{|D_b|} \sum_{\sigma_j \in D_b} \log \left| \frac{p_{\lambda}(\sigma_j)}{Z_{\lambda}} \right|. \quad (\text{C1})$$

Notice that because the calculation of \mathcal{L} requires the evaluation of intractable partition functions Z_{λ} , we restrict our calculation to small systems with $N = 20$ and $\alpha = 1$, where an exact evaluation of Z_{λ} is still possible. For a generic evaluation of Z_{λ} , one has to resort to advanced sampling techniques such as parallel tempering and annealed importance sampling.⁴³ From this perspective, overfitting would be evidenced by a continuous improvement of both the training and held-out \mathcal{L} followed by degradation of *only* the held-out \mathcal{L} due to the excessive adjustment of the parameters of the RBM that improves the \mathcal{L} of the training dataset exclusively. In Fig. 6(b) we display the evolution of the held-out \mathcal{L} as the training progresses. We also report the value of the held-out data set $\mathcal{L}_M = -\log N$ under the distribution it came from, i.e., the modulus square of the amplitudes in the W state, which is the optimal value the RBM would achieve if it perfectly described the data. Apart from noticing that no evidence of overfitting is found, we emphasize that the held-out \mathcal{L} approaches the theoretical value \mathcal{L}_M near the end of the training, which means that the RBM describes the distribution of the data remarkably well.

- ¹ Hinton, G. E. & Salakhutdinov, R. R. Reducing the Dimensionality of Data with Neural Networks. *Science* **313**, 504–507 (2006). URL <http://science.sciencemag.org/content/313/5786/504>.
- ² LeCun, Y., Bengio, Y. & Hinton, G. Deep learning. *Nature* **521**, 436–444 (2015). URL <http://www.nature.com/nature/journal/v521/n7553/full/nature14539.html>.
- ³ Wang, L. Discovering phase transitions with unsupervised learning. *Physical Review B* **94**, 195105 (2016). URL <http://link.aps.org/doi/10.1103/PhysRevB.94.195105>.
- ⁴ Carrasquilla, J. & Melko, R. G. Machine learning phases of matter. *Nature Physics advance online publication* (2017). URL <http://www.nature.com/nphys/journal/vaop/ncurrent/full/nphys4035.html>.
- ⁵ Broecker, P., Carrasquilla, J., Melko, R. G. & Trebst, S. Machine learning quantum phases of matter beyond the fermion sign problem. *arXiv:1608.07848* (2016). URL <http://arxiv.org/abs/1608.07848>.
- ⁶ van Nieuwenburg, E. P. L., Liu, Y.-H. & Huber, S. D. Learning phase transitions by confusion. *Nature Physics advance online publication* (2017). URL <http://www.nature.com/nphys/journal/vaop/ncurrent/full/nphys4037.html>.
- ⁷ Huang, L. & Wang, L. Accelerated Monte Carlo simulations with restricted Boltzmann machines. *Physical Review B* **95**, 035105 (2017). URL <http://link.aps.org/doi/10.1103/PhysRevB.95.035105>.
- ⁸ Liu, J., Qi, Y., Meng, Z. Y. & Fu, L. Self-learning Monte Carlo method. *Physical Review B* **95**, 041101 (2017). URL <http://link.aps.org/doi/10.1103/PhysRevB.95.041101>.
- ⁹ Carleo, G. & Troyer, M. Solving the quantum many-body problem with artificial neural networks. *Science* **355**, 602–606 (2017). URL <http://science.sciencemag.org/content/355/6325/602>.
- ¹⁰ Vogel, K. & Risken, H. Determination of quasiprobability distributions in terms of probability distributions for the rotated quadrature phase. *Physical Review A* **40**, 2847 (1989). URL <http://journals.aps.org/pra/abstract/10.1103/PhysRevA.40.2847>.
- ¹¹ Islam, R. *et al.* Measuring entanglement entropy in a quantum many-body system. *Nature* **528**, 77–83 (2015). URL <http://www.nature.com/nature/journal/v528/n7580/full/nature15750.html>.
- ¹² Cramer, M. *et al.* Efficient quantum state tomography. *Nature communications* **1**, 149–149 (2009). URL <http://www.nature.com/articles/ncomms1147>.
- ¹³ Lanyon, B. *et al.* Efficient tomography of a quantum many-body system. *arXiv preprint arXiv:1612.08000* (2016). URL <https://arxiv.org/abs/1612.08000>.
- ¹⁴ Torlai, G. & Melko, R. G. Learning thermodynamics with Boltzmann machines. *Physical Review B* **94**, 165134 (2016). URL <http://link.aps.org/doi/10.1103/PhysRevB.94.165134>.
- ¹⁵ Torlai, G. & Melko, R. G. A Neural Decoder for Topological Codes. *arXiv:1610.04238* (2016). URL <http://arxiv.org/abs/1610.04238>.
- ¹⁶ Deng, D.-L., Li, X. & Sarma, S. D. Exact Machine Learning Topological States. *arXiv:1609.09060* (2016). URL <http://arxiv.org/abs/1609.09060>.
- ¹⁷ Deng, D.-L., Li, X. & Sarma, S. D. Quantum Entanglement in Neural Network States. *arXiv:1701.04844* (2017). URL <http://arxiv.org/abs/1701.04844>.
- ¹⁸ Gao, X. & Duan, L.-M. Efficient Representation of Quantum Many-body States with Deep Neural Networks. *arXiv:1701.05039* (2017). URL <http://arxiv.org/abs/1701.05039>.

- ¹⁹ Chen, J., Cheng, S., Xie, H., Wang, L. & Xiang, T. On the Equivalence of Restricted Boltzmann Machines and Tensor Network States. *arXiv:1701.04831* (2017). URL <http://arxiv.org/abs/1701.04831>.
- ²⁰ Huang, Y. & Moore, J. E. Neural network representation of tensor network and chiral states. *arXiv:1701.06246* (2017). URL <http://arxiv.org/abs/1701.06246>. ArXiv: 1701.06246.
- ²¹ Häffner, H. *et al.* Scalable multiparticle entanglement of trapped ions. *Nature* **438**, 643–646 (2005). URL <https://www.nature.com/nature/journal/v438/n7068/abs/nature04279.html>.
- ²² Lanyon, B. P. *et al.* Efficient tomography of a quantum many-body system. *arXiv:1612.08000* (2016). URL <http://arxiv.org/abs/1612.08000>.
- ²³ Tóth, G. *et al.* Permutationally invariant quantum tomography. *Phys. Rev. Lett.* **105**, 250403 (2010). URL <https://link.aps.org/doi/10.1103/PhysRevLett.105.250403>.
- ²⁴ Lu, C.-Y. *et al.* Experimental entanglement of six photons in graph states. *Nature Physics* **3**, 91–95 (2007). URL <http://www.nature.com/nphys/journal/v3/n2/abs/nphys507.html>.
- ²⁵ Wang, X.-L. *et al.* Experimental Ten-Photon Entanglement. *Physical Review Letters* **117**, 210502 (2016). URL <https://link.aps.org/doi/10.1103/PhysRevLett.117.210502>.
- ²⁶ Richerme, P. *et al.* Non-local propagation of correlations in quantum systems with long-range interactions. *Nature* **511**, 198–201 (2014). URL <http://dx.doi.org/10.1038/nature13450>.
- ²⁷ Bakr, W. S. *et al.* Probing the superfluid-to-mott Insulator Transition at the Single-Atom Level. *Science* **329**, 547–550 (2010). URL <http://science.sciencemag.org/content/329/5991/547>.
- ²⁸ Hastings, M. B., González, I., Kallin, A. B. & Melko, R. G. Measuring Renyi Entanglement Entropy in Quantum Monte Carlo Simulations. *Physical Review Letters* **104**, 157201 (2010). URL <https://link.aps.org/doi/10.1103/PhysRevLett.104.157201>.
- ²⁹ Johnson, M. W. *et al.* Quantum annealing with manufactured spins. *Nature* **473**, 194–198 (2011). URL <http://www.nature.com/nature/journal/v473/n7346/full/nature10012.html>.
- ³⁰ Bloch, I., Dalibard, J. & Zwerger, W. Many-body physics with ultracold gases. *Reviews of Modern Physics* **80**, 885–964 (2008).
- ³¹ Blatt, R. & Roos, C. F. Quantum simulations with trapped ions. *Nature Physics* **8**, 277–284 (2012). URL <http://www.nature.com/nphys/journal/v8/n4/abs/nphys2252.html>.
- ³² Shulman, M. D. *et al.* Demonstration of Entanglement of Electrostatically Coupled Singlet-Triplet Qubits. *Science* **336**, 202–205 (2012). URL <http://science.sciencemag.org/content/336/6078/202>.
- ³³ Hinton, G. E. Training products of experts by minimizing contrastive divergence. *Neural Comput.* **14**, 1771–1800 (2002). URL <http://dx.doi.org/10.1162/089976602760128018>.
- ³⁴ Goodfellow, I., Bengio, Y. & Courville, A. *Deep Learning* (MIT Press, 2016). <http://www.deeplearningbook.org>.
- ³⁵ Amari, S.-i. Natural Gradient Works Efficiently in Learning. *Neural Computation* **10**, 251–276 (1998). URL <http://www.mitpressjournals.org/doi/10.1162/089976698300017746>.
- ³⁶ Sorella, S. Green function monte carlo with stochastic reconfiguration. *Physical review letters* **80**, 4558 (1998).
- ³⁷ Suzuki, M. Relationship between d-dimensional quantal spin systems and (d+1)-dimensional ising systemsequivalence, critical exponents and systematic approximants of the partition function and spin correlations. *Progress of Theoretical Physics* **56**, 1454 (1976).
- ³⁸ Wolff, U. Collective monte carlo updating for spin systems. *Phys. Rev. Lett.* **62**, 361–364 (1989).
- ³⁹ Rieger, H. & Kawashima, N. Application of a continuous time cluster algorithm to the two-dimensional random quantum ising ferromagnet. *The European Physical Journal B - Condensed Matter and Complex Systems* **9**, 233–236 (1999). URL <http://dx.doi.org/10.1007/s100510050761>.
- ⁴⁰ Mazzola, G. & Troyer, M. Quantum monte carlo annealing with multi-spin dynamics. *Journal of Statistical Mechanics: Theory and Experiment* **2017**, 053105 (2017).
- ⁴¹ Evertz, H. G. The loop algorithm. *Advances in Physics* **52**, 1–66 (2003). URL <http://dx.doi.org/10.1080/0001873021000049195>.
- ⁴² Krzakala, F., Rosso, A., Semerjian, G. & Zamponi, F. Path-integral representation for quantum spin models: Application to the quantum cavity method and monte carlo simulations. *Phys. Rev. B* **78**, 134428 (2008). URL <https://link.aps.org/doi/10.1103/PhysRevB.78.134428>.
- ⁴³ Salakhutdinov, R. & Murray, I. On the quantitative analysis of deep belief networks. In *Proceedings of the International Conference on Machine Learning*, vol. 25 (2008).